(Received 9 February 2026, Accepted 25 March 2026, Scheduled 7 May 2026)

Study on the Transmission Characteristics of a WPT System with Double Semicircular Coplanar Coils

Suqi Liu[1,*], Changxin Guo[1], Xinying Zhou[1], Gang Wang[1], and Yuping Liu[2]

[1] College of Mechanical and Electrical Engineering, Guilin University of Electronic Technology, Guilin 541004, China
[2] College of Electronic Engineering and Automation, Guilin University of Electronic Technology, Guilin 541004, China

ABSTRACT: For small, low-power wireless power transfer (WPT) devices, maintaining constant output power and high transmission efficiency over a wide range of coupling variations remains a significant challenge. The double semicircular coplanar (DSC) coils, featuring unique magnetic field distribution, provide a potential solution for enhancing misalignment tolerance. This paper analyzes the transmission characteristics of a WPT system employing DSC coils. A circuit model for the WPT system with DSC coils is first developed, and its fundamental transmission characteristics are studied. The tolerance of output power and transmission efficiency to positional offsets (X, Y, Z) over various frequency bands is then evaluated. Finally, an experimental DSC coil system that features a stable frequency bandwidth and is largely insensitive to frequency shifts is built. Its misalignment tolerance forms a cuboid spatial zone. Within this zone, namely, when the offset of the receiver in X and Y is under half its diameter, the output power and transmission efficiency remain constant, supported by a uniform magnetic field. When the receiver offset is greater than half its diameter, the magnetic field uniformity and mutual inductance change abruptly, leading to a sudden variation in output power and transmission efficiency.

1. INTRODUCTION

Since Nikola Tesla's early-20th-century study [1], the wireless power transfer (WPT) technology has seen a significant progress. The emergence of magnetically coupled resonant WPT [2] led to its broad adoption in various fields, including consumer electronics, electric vehicles, and household appliances [3, 4].

While conventional coil topologies, such as circular and square spiral coils, are structurally simple and manufacturing-mature, they have significant limitations. In fact, the magnetic field of a circular coil exhibits a large decay with distance, which results in significantly decreasing the short-range transmission efficiency. On the contrary, the field at the edges of a square coil abruptly changes, which makes the system highly susceptible to positional deviation. These characteristics make the two types unsuitable for dynamic applications that require high misalignment tolerance [5].

To enhance the system tolerance to misalignment, studies have mainly focused on coil topology innovation and compensation topology optimization. For instance, Kalwar et al. [6] proposed a Quadrature Double-D (QDQ) coil structure combined with a Series-Series (SS) compensation network. Their design integrates four adjacent circular coils with a square coil, allowing for efficient energy transmission even at a misalignment displacement of 50% of the coil size. Prosen et al. [7] conducted an in-depth study on the double DD coil structure. Their results verified its advantages in increasing the power density and enhancing the offset tolerance. Domajnko and Prosen [8] then introduced a Double-D (DD) quadrature coil structure, which adds a set of non-polarized orthogonal coils at the transmitter and receiver. Their results showed that this structure increases the power density of the system while significantly enhancing its misalignment tolerance. Domajnko and Prosen [9] addressed coil rotation misalignment by optimizing the layout of transmitting and receiving coils. This allowed for enhancing the tolerance of the system to the Z-axis rotation and to solve the problem of the decrease in the coupling coefficient in conventional DD coils. Xie et al. [10] also presented a fully integrated WPT system with an LCCL-S compensation topology that employs an extended DD coil as compensation inductance. Their results showed that this approach achieves over 63.6% steady-state efficiency at an offset of 150 mm. Abdulhameed et al. [11] tackled dynamic charging by proposing a wireless charger with LCC compensation for electric vehicles powered by roads. This solution integrates multiple inductive links on the secondary side, each with independent DD quadrature coils, presenting a novel approach for such applications.

It can be deduced from the aforementioned analysis that the double semicircular coplanar (DSC) coils leverage their unique magnetic field distribution and structural symmetry for generating a distinctive horizontal magnetic field through a specific dual-coil arrangement. This configuration increases the transmission efficiency and exhibits inherent tolerance to positional misalignment, demonstrating its high potential for anti-offset applications. The DSC structure introduces significant theoretical innovations over existing coil topologies.

The DD coil improves the lateral offset tolerance through a bipolar magnetic field. However, its unidirectional field distribution leads to much lower offset tolerance in the vertical direction. The Double-D Quadrature (DDQ) coil increases the offset

* Corresponding author: Suqi Liu (liusuqi2009@126.com).

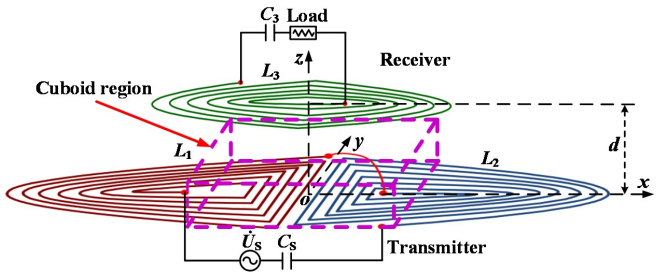

FIGURE 1. Sketch of the WPT system with DSC (M-Tx, S-Tx, and receiver (Rx)) coils.

performance by adding orthogonal coils, which comes at the expense of increased structural complexity and higher frequency sensitivity. On the contrary, the DSC coil employs a symmetrical semi-circular coplanar design that generates a more uniform spatial magnetic field without requiring additional orthogonal components. Thus, it achieves superior three-dimensional (3D) offset tolerance and frequency insensitivity while retaining a simpler and more compact structure. However, to the best of our knowledge, a systematic model and an experimental validation for this topology do not exist.

This paper tackles DSC coils as a coupled topology. It first develops a circuit model to analyze power transfer characteristics. A 3D electromagnetic simulation model is developed in ANSYS Electronics 2021 R1 to evaluate the anti-misalignment capability and magnetic field uniformity at three frequency bands: 191, 196, and 201 kHz. An experimental setup is then established to validate the simulated and theoretical results, providing theoretical basis and parametric guidance for the applications of DSC coils in WPT.

The obtained results demonstrate that, at the specified frequency bands, stable output power and transmission efficiency can be maintained when the displacement of the receiver in the X and Y directions is less than half of its outer diameter. The main contributions of this paper are summarized as follows:

(1) A novel DSC coil topology for small, low-power WPT devices is proposed.

(2) The developed system features high frequency insensitivity and enhanced misalignment tolerance within a cuboid region.

(3) Several improved coil structures, featuring high transmission performance, are provided.

The remainder of this paper is organized as follows. Section 2 presents the theoretical modeling and analysis of the DSC coils, including the derivation of its transmission characteristics. Section 3 details the analysis of the impact of the coupling misalignment on the output power and transmission efficiency. Section 4 presents the experimental results. Section 5 outlines the associated technology and applications of the DSC coils. Finally, the conclusion is drawn in Section 6.

2. MODELING OF THE WPT SYSTEM WITH DSC COILS

It has been demonstrated that the use of two transmitter coils generates a uniform magnetic field, maintaining constant output power and high transmission efficiency at a fixed frequency [12, 13]. In this paper, a WPT system topology that incorporates DSC coils is proposed, and its transmission characteristics are analyzed.

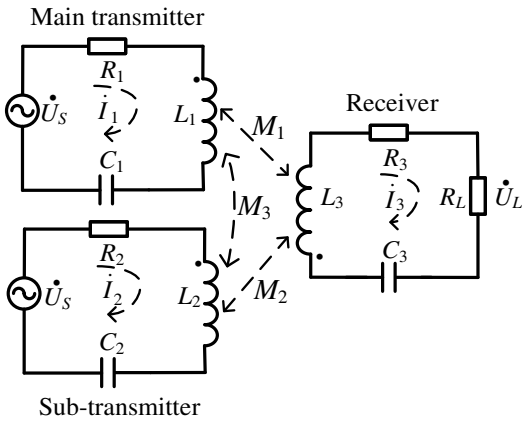

FIGURE 2. Equivalent circuit of the WPT system with DSC coils.

To obtain constant output power and transmission efficiency, a single-load WPT model with DSC coils is first developed.

Figure 1 presents its schematic, comprising two transmitter coils (L_1, L_2) and a receiver coil (L_3). In this setup, the DSC coils are linked into the transmitter loop. Using the same transmitter circuit, the main transmitter (M-Tx) and sub-transmitter (S-Tx) loops are formed. Fig. 2 shows the equivalent circuit of the WPT system with DSC coils.

The DSC coils are placed horizontally on the plane, and their vertical segments are aligned side by side. A coordinate system is established. The midpoint of the intersection line of the two transmitting coils is considered as the origin. The vertical plane that contains the two transmitting coils is the Z-plane, while the upward direction along their intersection line is the Y-axis. The X-axis lies in the horizontal plane, perpendicular to the intersection line and passing through the origin.

The parameters of the WPT system with DSC coils are presented in Table 1. An equivalent circuit model is then developed to facilitate the analysis of the transmission characteristics of the system. The corresponding parameters assumed for the M-Tx, S-Tx, and Rx coils in this model are shown in Table 2.

TABLE 1. Parameters of the WPT system with DSC coils.

Parameter	Value
Input power	$\dot{U}_S$
Load voltage	$\dot{U}_L$
Winding ohmic resistance of the coil	R_1, R_2, R_3
Load resistance	R_L
Inductance of the coil	L_1, L_2, L_3
Capacitance	C_1, C_2, C_3
Mutual inductance	M_1, M_2, M_3

TABLE 2. Assumed values for the individual circuit elements of the M-Tx, S-Tx, and Rx coils.

Parameter	Value
Capacitances	$C_S = C_1 = C_2 = C_3$
Inductances	$L_1 = L_2 = L_3$
Resistance	$R_3 + R_L = R$
Ratio	$R_L = \beta R$, $R_1 = R_2 = \sigma R$ (σ >0)
Driving angular frequency	ω
Resonance frequency	$f_0 = \omega_0/2\pi$
Frequency detuning factor	$\xi = Q_0(\omega/\omega_0 - \omega_0/\omega)$
Resonant angular frequency	$\omega_0 = 1/(LC)^{0.5}$, $\omega_1 = \omega_2 = \omega_3 = \omega_0$
Quality factor	$Q_0 = \omega_0 L/R = 1/(\omega_0 CR)$, $Q_1 = Q_2 = \omega_0 L/R_1 = 1/(\omega_0 CR_1) = Q_0/\sigma$

The WPT system with M-Tx, S-Tx, and Rx coils can be expressed as:

$$\begin{cases} Z_1\dot{I}_1 - j\omega M_1\dot{I}_3 - j\omega M_3\dot{I}_2 = \dot{U}_S \\ Z_2\dot{I}_2 - j\omega M_2\dot{I}_3 - j\omega M_3\dot{I}_1 = \dot{U}_S \\ Z_3\dot{I}_3 - j\omega M_1\dot{I}_1 - j\omega M_2\dot{I}_2 = 0 \end{cases} \tag{1}$$

The Z_1, Z_2, and Z_3 self-impedances are given by [14, 15]:

$$\begin{cases} Z_1 = Z_2 = R_1 + j\omega L_1 + \frac{1}{j\omega C_S} \\ = (\sigma + \frac{j\omega_0 L}{R}\frac{\omega}{\omega_0} + \frac{1}{j\omega_0 CR}\frac{\omega_0}{\omega})R = (\sigma + j\xi)R \\ Z_3 = R_3 + R_L + j\omega L_3 + \frac{1}{j\omega C_3} \\ = (1 + \frac{j\omega_0 L}{R}\frac{\omega}{\omega_0} + \frac{1}{j\omega_0 CR}\frac{\omega_0}{\omega})R = (1 + j\xi)R \end{cases} \tag{2}$$

where τ_1, τ_2, and τ_3 are the impedance coupling factors indicating the ability of impedance coupling [14, 15]:

$$\begin{cases} \tau_1 = \frac{\omega M_1}{\sqrt{R_1(R_3+R_L)}} = \frac{\omega M_1}{\sqrt{\sigma}R}, \quad \tau_1 > 0 \\ \tau_2 = \frac{\omega M_2}{\sqrt{R_2(R_3+R_L)}} = \frac{\omega M_2}{\sqrt{\sigma}R}, \quad \tau_2 > 0 \\ \tau_3 = \frac{\omega M_3}{\sqrt{R_1 R_2}} = \frac{\omega M_3}{\sigma R}, \quad \tau_3 > 0 \end{cases} \tag{3}$$

Based on Equation (3), the mutual inductance expression of each circuit can be written as:

$$\begin{cases} M_1 = \frac{\tau_1\sqrt{\sigma}R}{\omega}, \quad \tau_1 > 0 \\ M_2 = \frac{\tau_2\sqrt{\sigma}R}{\omega}, \quad \tau_2 > 0 \\ M_3 = \frac{\tau_3\sigma R}{\omega}, \quad \tau_3 > 0 \end{cases} \tag{4}$$

Using Equations (1)–(3) and the parameters presented in Table 2, the currents can be expressed as:

$$\begin{cases} \dot{I}_1 = \dfrac{\begin{matrix}(\sigma+j\xi)(1+j\xi)^2 + (1+j\xi)\tau_2^2\sigma \\ +j\tau_3^2\sigma^2(1+j\xi) - \tau_1\tau_2\sigma(1+j\xi)\end{matrix}}{\begin{matrix}(\sigma+j\xi)^2(1+j\xi)^2 + \tau_1^2\sigma(\sigma+j\xi)(1+j\xi) \\ +\tau_2^2\sigma(\sigma+j\xi)(1+j\xi) + \tau_3^2\sigma^2(1+j\xi)^2 + j2\tau_1\tau_2\tau_3\sigma^2\end{matrix}}\frac{U_S}{R} \\ \dot{I}_2 = \dfrac{\begin{matrix}(\sigma+j\xi)(1+j\xi)^2 + (1+j\xi)\tau_1^2\sigma \\ +j\tau_3^2\sigma^2(1+j\xi) - \tau_1\tau_2\sigma(1+j\xi)\end{matrix}}{\begin{matrix}(\sigma+j\xi)^2(1+j\xi)^2 + \tau_1^2\sigma(\sigma+j\xi)(1+j\xi) \\ +\tau_2^2\sigma(\sigma+j\xi)(1+j\xi) + \tau_3^2\sigma^2(1+j\xi)^2 + j2\tau_1\tau_2\tau_3\sigma^2\end{matrix}}\frac{U_S}{R} \\ \dot{I}_3 = j\dfrac{\begin{matrix}(\tau_1+\tau_2)\sqrt{\sigma}(\sigma+j\xi)(1+j\xi) + (\tau_1+\tau_2)\tau_1\tau_2\sigma\sqrt{\sigma} \\ +j(\tau_1+\tau_2)\tau_3^2\sigma^2\sqrt{\sigma} - (\tau_1+\tau_2)\tau_1\tau_2\sigma\sqrt{\sigma}\end{matrix}}{\begin{matrix}(\sigma+j\xi)^2(1+j\xi)^2 + \tau_1^2\sigma(\sigma+j\xi)(1+j\xi) \\ +\tau_2^2\sigma(\sigma+j\xi)(1+j\xi) + \tau_3^2\sigma^2(1+j\xi)^2 + j2\tau_1\tau_2\tau_3\sigma^2\end{matrix}}\frac{U_S}{R} \end{cases} \tag{5}$$

The output power (P_{out}) and transmission efficiency (η) are calculated using Equation (5):

$$\begin{aligned} P_{out} = |\dot{I}_3|^2 R_L = \beta\sigma(\tau_1+\tau_2)^2[(\sigma-\xi^2)^2 + (\sigma\xi+\xi+\tau_3^2\sigma^2)^2]/ \\ [(\sigma^2 - \xi^2 - 4\sigma\xi^2 - \sigma^2\xi^2 + \xi^4 + \tau_1^2\sigma^2 + \tau_2^2\sigma^2 \\ +\tau_3^2\sigma^2 - \tau_1^2\xi^2\sigma - \tau_2^2\xi^2\sigma - \tau_3^2\xi^2\sigma^2)^2 \\ +(2\sigma\xi + 2\xi\sigma^2 - 2\xi^2 - 2\sigma\xi^3 + \tau_1^2\sigma^2\xi + \tau_2^2\sigma^2\xi \\ +\tau_1^2\sigma\xi + \tau_2^2\sigma\xi + 2\tau_3^2\sigma^2\xi + 2\tau_1\tau_2\tau_3\sigma^2)^2] \end{aligned} \tag{6}$$

$$\begin{aligned} \eta = \frac{P_{out}}{P_{in}} = \frac{|\dot{I}_3|^2 R_L}{|\dot{I}_1|^2 R_1 + |\dot{I}_2|^2 R_2 + |\dot{I}_3|^2 (R_3 + R_L)} \\ = \beta(\tau_1+\tau_2)^2[(\sigma-\xi^2)^2 + (\sigma\xi+\xi+\tau_3^2\sigma^2)^2]/ \\ \{(\sigma - \sigma\xi^2 - 2\xi^2 + \tau_2^2\sigma - \tau_3^2\sigma^2\xi - \tau_1\tau_2\sigma)^2 \\ +(2\sigma\xi + \xi - \xi^3 + \xi\tau_2^2\sigma + \tau_3^2\sigma^2 - \xi\tau_1\tau_2\sigma)^2 \\ +(\sigma - \sigma\xi^2 - 2\xi^2 + \tau_1^2\sigma - \tau_3^2\sigma^2\xi - \tau_1\tau_2\sigma)^2 \\ +(2\sigma\xi + \xi - \xi^3 + \xi\tau_1^2\sigma + \tau_3^2\sigma^2 - \xi\tau_1\tau_2\sigma)^2 \\ +(\tau_1+\tau_2)^2[(\sigma-\xi^2)^2 + (\sigma\xi+\xi+\tau_3^2\sigma^2)^2]\} \end{aligned} \tag{7}$$

3. ANALYSIS OF THE WPT SYSTEM WITH DSC COILS

3.1. Simulation and Analysis of Magnetic Field Distribution

The 3D electromagnetic model of the WPT system with DSC coils, developed using the ANSYS finite element simulation software is shown in Fig. 3. The model uses the coil parameters presented in Table 3, while key quantities, such as the inductance and capacitance of the M-Tx, S-Tx, and Rx coils, remain consistent, and the number of turns is uniformly set to 10. This ensures high accuracy of the simulation results and their value for engineering reference. In the simulation, balloon boundary conditions are applied to mimic an infinite space environment,

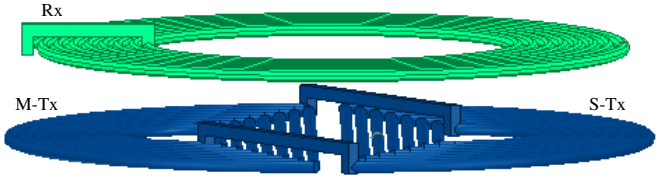

FIGURE 3. Model of the WPT system with DSC coils.

TABLE 3. Parameters used in the simulation of the WPT system with DSC coils.

Parameter	M-Tx or S-Tx coil	Rx coil
Inductance L/μH	29.25	29.25
Capacitance C/nF	44.18	44.18
Outside diameter of the coil Φ/mm	40	39
Inside diameter of the coil φ/mm	14	3
Operating frequency f/kHz	191/196/201	191/196/201
Current I/A	1.5	1.5
Number of turns	10	10
Material	copper	
Impedance scaling factor σ	0.5	
Frequency detuning factor ξ	0.262	
Load R_L/Ω	0.5	
Input power P_{in}/W	34.4	
Input voltage U_S/V	17.8	
Solution type	Eddy current	
Number of model elements	10000	
Maximum element length/mm	0.4	
Maximum iterations	10	
Percent error	0.5%	
Refinement per pass	30%	
Region	300 in x, y and z	

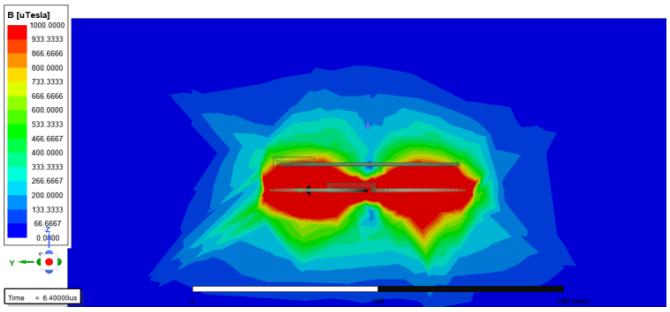

FIGURE 4. Magnetic field distribution in the YZ plane for the 191 kHz model of the WPT system with DSC coils.

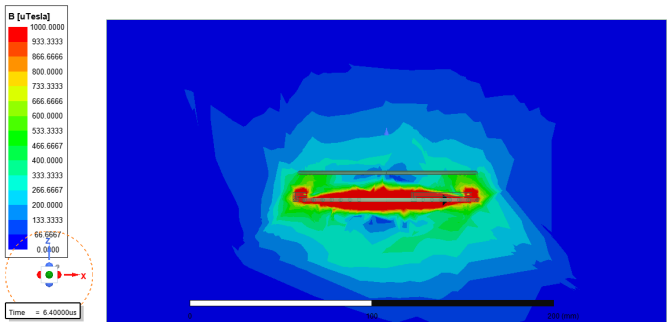

FIGURE 5. Magnetic field distribution in the XZ plane for the 191 kHz model of the WPT system with DSC coils.

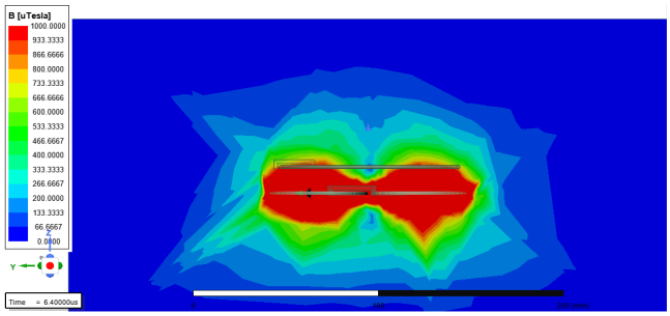

FIGURE 6. Magnetic field distribution in the YZ plane for the 196 kHz model of the WPT system with DSC coils.

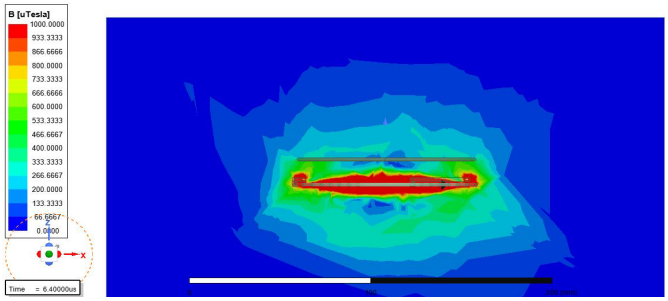

FIGURE 7. Magnetic field distribution in the XZ plane for the 196 kHz model of the WPT system with DSC coils.

allowing for removing the interference induced by boundary reflections on the magnetic field distribution. The surrounding medium is defined as air with a relative permeability (μ_r) of 1 to closely reproduce the electromagnetic conditions in real application scenarios.

WPT systems exhibit frequency splitting. Thus, in the over-coupled region [14], three operating frequencies are selected: 196 kHz as the resonant frequency, 191 kHz and 201 kHz as the lower and higher frequencies, respectively. The distributions of the magnetic field at these frequencies are analyzed and compared through simulation. The obtained results are shown in Figs. 4–9. It can be seen that the field morphology and intensity do not exhibit a significant variation in this frequency range. A closed magnetic induction loop is established between the semicircular coils of the DD structure, confining the area of high field strength primarily to the inner side of the transceiver coils. A weaker field distribution outside the coils indicates the presence of magnetic leakage. A stable magnetic field region, approximating a cuboid in shape, exists at the spatial coordinates of $X = \pm 20$ mm, $Y = \pm 20$ mm, and $Z = 0$–15 mm. This stable region confirms, at the magnetic field level, the theoretical foundation of the anti-misalignment capability of the system.

It can be deduced from the aforementioned analysis that the magnetic field in the frequency band of 191–201 kHz remains almost stable. This is highlighted by the observed region of a stable magnetic field having an approximately rectangular shape, located at $x = \pm 20$ mm, $y = \pm 20$ mm, and $z = 0$–15 mm. The high field intensity is intense in the coupling region, facilitating the efficient transmission of energy.

However, existing edge leakage may yield losses in efficiency, and thus it should be minimized through shielding or

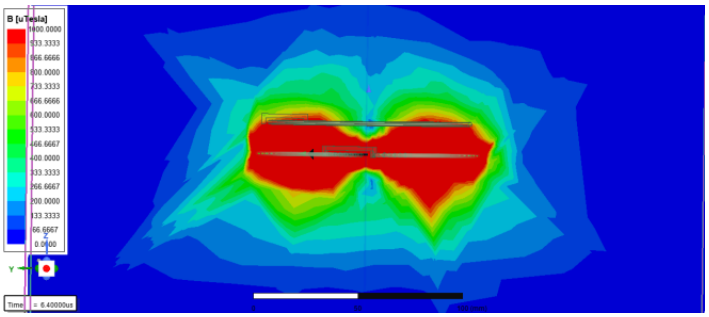

FIGURE 8. Magnetic field distribution in the YZ plane for the 201 kHz model of the WPT system with DSC coils.

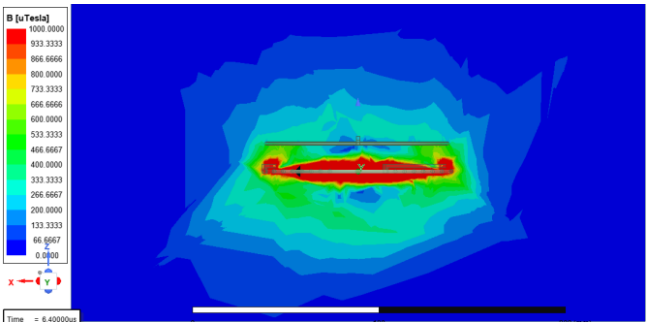

FIGURE 9. Magnetic field distribution in the XZ plane for the 201 kHz model of the WPT system with DSC coils.

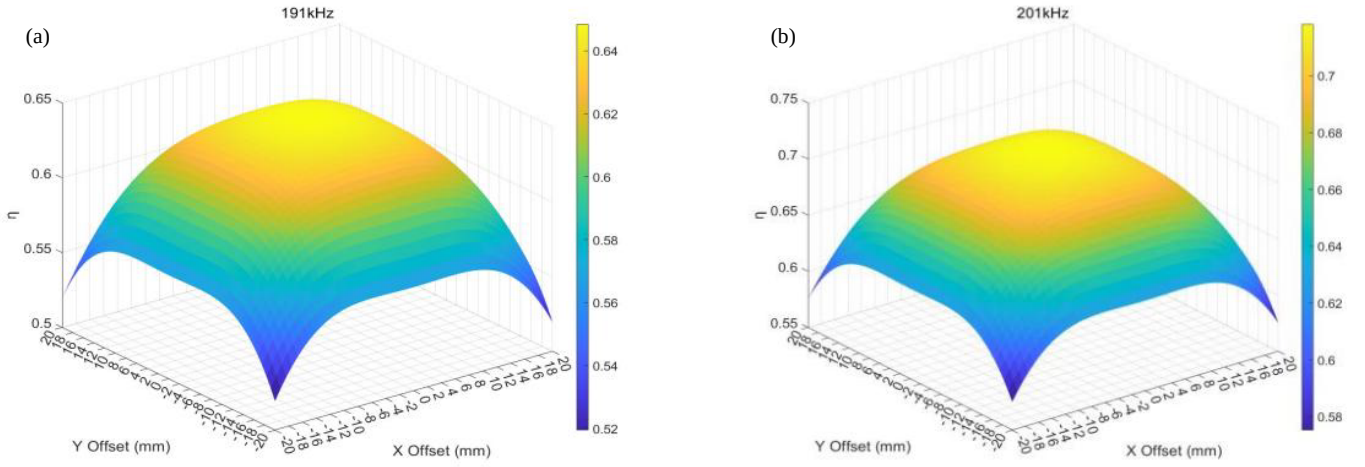

FIGURE 10. Characteristics of η of the WPT system with DSC coils at $Z = 15$ mm: simulated η distribution at (a) 191 kHz and (b) 201 kHz.

spacing optimization. The magnetic field direction shows high consistency, which helps reduce eddy current losses allowing for meeting the requirements for high-efficiency transmission. It is important to mention that the current model does not account for the impact of the temperature increase on the material properties. Therefore, in future work, multi-physics field coupling analysis should be conducted to address this limitation.

3.2. Simulation and Analysis of the Output Power and Transmission Efficiency

The transmission efficiency (η) (cf. Equation (7)) is determined by five key factors: β, σ, ξ, τ_1, and τ_2. Therefore, a MATLAB model incorporating the parameters presented in Table 3 is developed to study the characteristics of η. The obtained results are shown in Fig. 10.

It can be seen that η of the coil has a stable trend in the frequency band of 191–201 kHz, demonstrating that the system is insensitive to frequency. Note that this conclusion will be combined with the analysis of the following experimental results to determine the final ones.

In summary, the simulation results demonstrate that the WPT system with DSC coils exhibits a "high-coupling, low-leakage" magnetic field distribution, and it maintains a stable η over the operational frequency band. These attributes are conducive to energy transfer under the given parameters. However, they leave room for further optimization. Thus, in future work, the misalignment tolerance and magnetic field uniformity of the system will be experimentally validated.

4. EXPERIMENTAL RESULTS

The block diagram of the experimental WPT system with DSC coils is illustrated in Fig. 11. An AC 220 V input is used, with the following labeled components: capacitors C_S and C_3, rectifier diodes D_1–D_4, load resistance R_L, and load voltage U_K.

The experimental setup for the system is shown in Fig. 12. It comprises a power amplifier, a function generator, voltage probes, an oscilloscope, capacitors, a transmitter, a receiver, a load, and the M-Tx, S-Tx, and Rx coils.

In the experimental system, a function generator produces a sinusoidal signal (cf. Figs. 11 and 12). A power amplifier is used to amplify the signal, which is input into the resonant circuit, generating an oscillating magnetic field. When the Rx coil is placed in this field, a high-frequency alternating current is induced. This current is then rectified and finally provided to the load for consumption.

In this experiment, the controlled variable method is employed. The operating frequency of the WPT system is constant at 191, 196, and 201 kHz. For each frequency, the output power

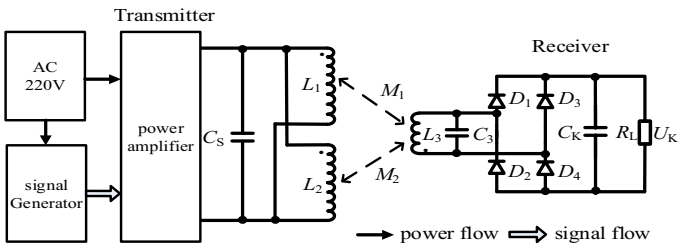

FIGURE 11. Experimental block diagram of the WPT system with DSC coils.

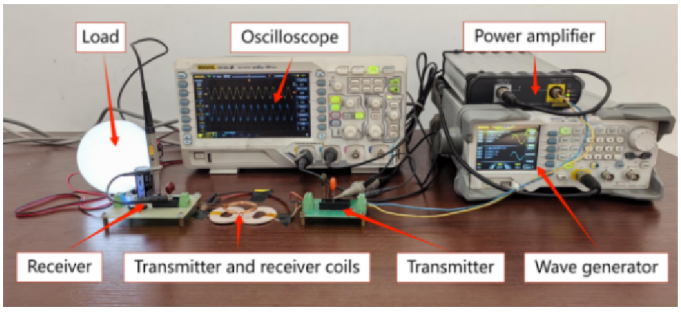

FIGURE 12. Experimental setup of the WPT system with DSC coils.

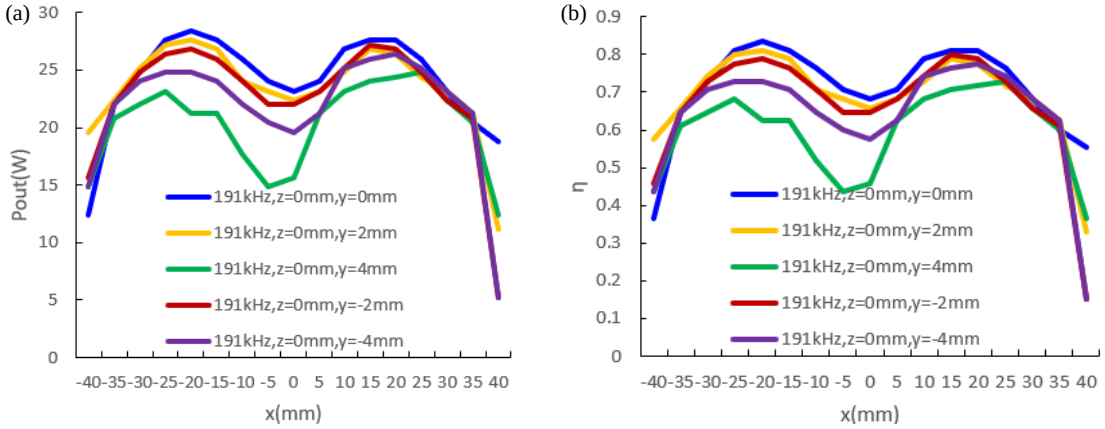

FIGURE 13. Characteristic curves of (a) output power and (b) η in the X-direction at $f = 191$ kHz and $Z = 0$ mm.

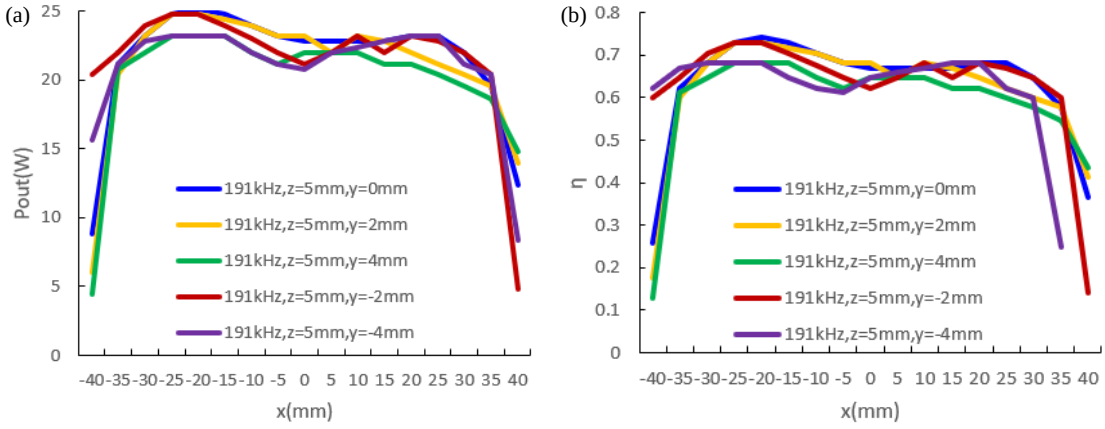

FIGURE 14. Characteristic curves of (a) output power and (b) η in the X-direction at $f = 191$ kHz and $Z = 5$ mm.

of the system is measured while the receiving coil is offset in the ranges of -40– $+40$ mm, -40–$+40$ mm, and 0–15 mm along the X, Y, and Z axes, respectively.

4.1. Transmission Characteristics of the WPT System with DSC Coils in the *X*-direction

To study the X-axis transmission characteristics of the WPT system, an experiment is conducted with the following fixed parameters: frequencies of 191, 196, and 201 kHz, and vertical gaps (Z) of 0, 5, 10, and 15 mm. Each configuration employs the following procedure.

With the Y-axis position fixed at -4 mm, the receiving coil is first displaced along the X-axis from -40 mm to $+40$ mm in increments of 5 mm, and the output power is recorded at each point. This X-axis sweep is then repeated at Y-axis positions of -2, 0, $+2$, and $+4$ mm (i.e., in increments of 2 mm). The results of these measurements are presented in Figs. 13–18. It can be seen that:

(1) At a frequency of 191 kHz, with Z set to 0, 5, 10, and 15 mm and Y incremented in steps of 2 mm, the output power remains stable within the lateral range of $X = \pm 30$ mm. In particular, it respectively records values of 22, 22, 22, and

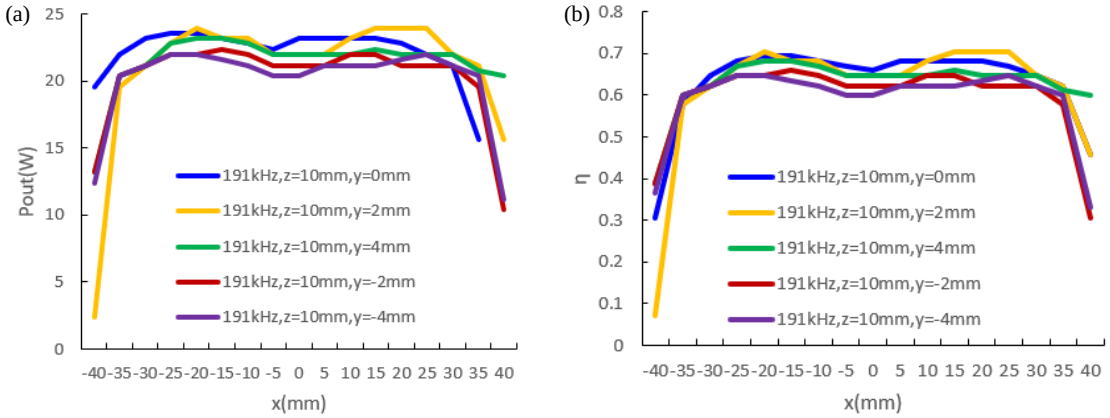

FIGURE 15. Characteristic curves of (a) output power and (b) η in the X-direction at $f = 191$ kHz and $Z = 10$ mm.

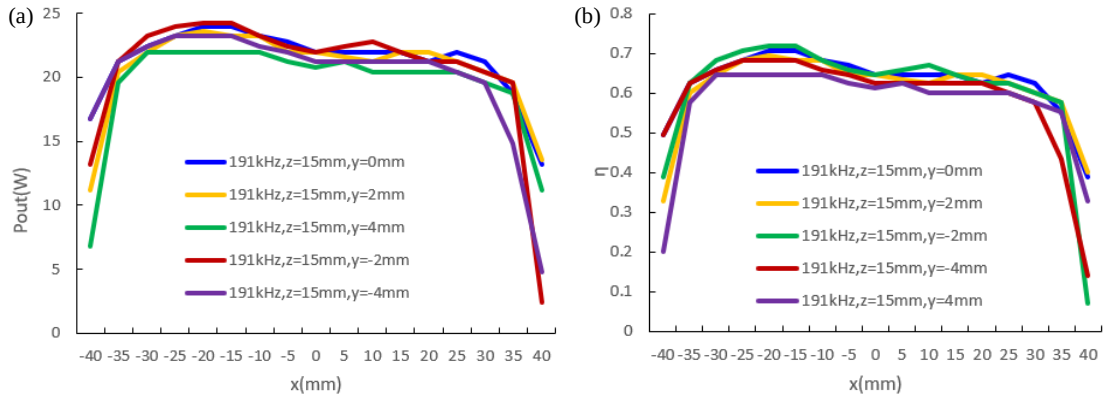

FIGURE 16. Characteristic curves of (a) output power and (b) η in the X-direction at $f = 191$ kHz and $Z = 15$ mm.

21 W, before sharply decreasing. The global maximum power is 25.2 W at ($X = -20$ mm, $Y = 0$ mm) for $Z = 0$ mm and $Z = 5$ mm, while it is 24 W at ($X = 15$ mm, $Y = 2$ mm) for $Z = 10$ mm, and 24.4 W at ($X = -20$ mm, $Y = -2$ mm) for $Z = 15$ mm. This demonstrates that an appropriate lateral offset can effectively optimize the coupling performance, as shown in Figs. 13–16.

(2) At a frequency of 196 kHz, with Z set to 0, 5, 10, and 15 mm and Y incremented in increments of 2 mm, the output power exhibits distinct stability regions for each Z setting. In particular, at $Z = 0$ mm, the output power remains stable at 20 W within $X = \pm 20$ mm, before sharply decreasing, and the global maximum power of 28.4 W is located at $X = -15$ mm, $Y = 0$ mm. At $Z = 5$ mm, stability is maintained at 20 W for $X = \pm 25$ mm, with a sharp decrease outside this range, while the global maximum power of 26.8 W occurs at $X = -20$ mm, $Y = 0$ mm. At $Z = 10$ mm, the output power remains stable at 20 W within $X = \pm 25$ mm, before sharply decreasing, and the global maximum power of 24 W occurs at $X = 10$ mm, $Y = 0$ mm, Finally, at $Z = 15$ mm, the output power is stable at 21 W across a wider range of $X = \pm 30$ mm, with a sharp decrease outside it, and the global maximum power of 22.4 W occurs at $X = 10$ mm, $Y = 0$ mm. These results demonstrate that an appropriate lateral offset can optimize the coupling performance. This is highlighted in Fig. 17 and presented at $Z = 15$ mm.

(3) At a frequency of 201 kHz, with Z set to 0, 5, 10, and 15 mm and Y incremented in steps of 2 mm, the output power remains stable within the lateral range of $X = \pm 30$ mm. In particular, it respectively records values of 23, 22, 22, and 21 W, before it sharply decreases. The global maximum power is 24.8 W at $X = -25$ mm, $Y = 0$ mm) for $Z = 5$ mm, 23.6 W at the same position for $Z = 10$ mm, and 23.2 W at ($X = -15$ mm, $Y = 0$ mm) for $Z = 15$ mm. These results demonstrate that an appropriate lateral offset can effectively optimize the coupling performance. This is highlighted in Fig. 18 and presented at $Z = 15$ mm.

4.2. Transmission Characteristics of the WPT System with DSC Coils in the *Y*-Direction

To study the transmission characteristics of the WPT system along the Y-direction, experiments are conducted at frequencies of 191, 196, and 201 kHz, while Z is set to 0, 5, 10, and 15 mm. The X-axis position is fixed at -4 mm, while the Y-axis position is varied in the range of -40–40 mm in increments of 5 mm. In addition, the X-direction is offset by -2, 0, 2, and 4 mm. For each X-offset, the Y-direction sweep is repeated, and the output voltage is measured and recorded. The obtained results are shown in Figs. 19–24. It can be observed that:

(1) At a frequency of 191 kHz, with Z set to 0, 5, 10, and 15 mm and the Y-direction offset incremented in steps of

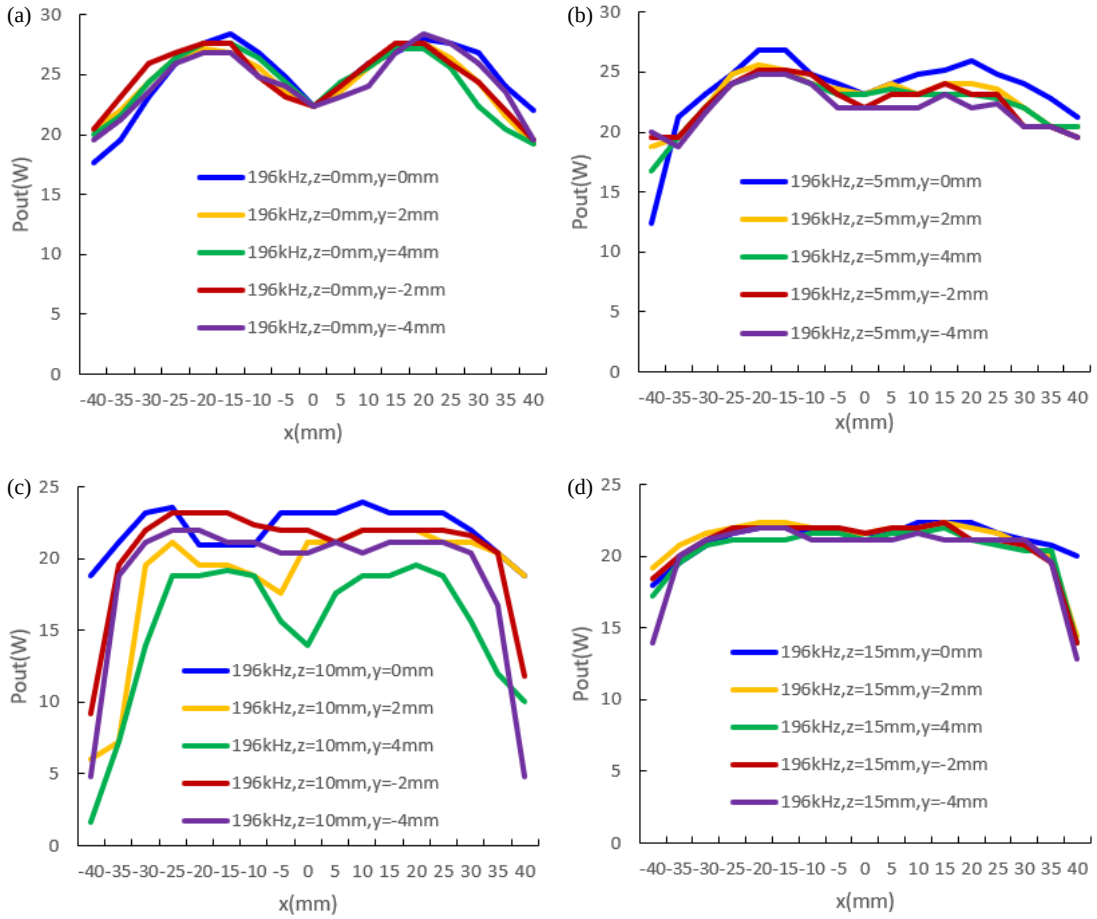

FIGURE 17. System output power characteristic curves under X-direction offset for (a) $Z = 0$ mm, (b) $Z = 5$ mm, (c) $Z = 10$ mm, and (d) $Z = 15$ mm, at $f = 196$ kHz.

2 mm, the output power remains stable within the range of $Y = \pm 20$ mm. In particular, it records values of 22, 22, 22, and 22 W, respectively. Near $Y = \pm 20$ mm, the power first decreases and then increases. This sharp transition may be attributed to magnetic field distortion resulting from the gap between the two semicircular coils. The maximum power occurs at 24.8 W ($Y = 0$ mm, $X = -4$ mm) for $Z = 0$ mm, 24.8 W ($Y = 5$ mm, $X = -4$ mm) for $Z = 5$ mm, 23.2 W ($Y = 0$ mm, $X = -4$ mm) for $Z = 10$ mm, and 23.2 W ($Y = 0$ mm, $X = -4$ mm) for $Z = 15$ mm. These results demonstrate that an appropriate lateral offset can increase the coupling performance (cf. Figs. 19–22).

(2) At the operating frequency of 196 kHz, with Z set to 0, 5, 10, and 15 mm, the output power remains stable within a Y-direction offset range of ± 20 mm, measured in increments of 2 mm. The corresponding steady-state output power values are fixed at 22 W, with fluctuation rates of approximately 9, 9, 4, and 13%, respectively. Beyond $Y = \pm 20$ mm, the output power sharply decreases, which demonstrates a significant coupling degradation. This may be attributable to the offset exceeding the effective spatial range of the coil structure. The global maximum power for each Z setting occurs at $Y = 0$ mm, $X = -4$ mm, with values of 27.6, 24.4, 23.6, and 23.2 W at $Z = 0$, 5, 10, and 15 mm, respectively. These results demonstrate that an appropriate lateral offset can optimize η. The output power profiles are illustrated in Fig. 23.

(3) When operating at 201 kHz with Z set to 0, 5, 10, and 15 mm, the output power remains stable within a Y-direction offset range of ± 20 mm, measured in increments of 2 mm. The corresponding steady-state output power values are 22 W, with fluctuation rates of approximately 22, 13, 9, and 9%, respectively. Beyond $Y = \pm 20$ mm, the power sharply decreases, demonstrating a significant coupling loss. This may be because the offset exceeds the effective spatial range of the coil system. The global maximum power occurs at $Y = 0$ mm, $X = -4$ mm, with values of 27.2, 25.2, 24.4, and 23.2 W at $Z = 0$, 5, 10, and 15 mm, respectively. These results demonstrate that a controlled lateral offset can increase the coupling efficiency. The corresponding output power profiles are presented in Fig. 24.

4.3. Comparison between the Efficiencies of Topological Structures

It can be deduced from Tables 4 and 5 that the stable operating range of output power exhibits clear 3D spatial distribution characteristics.

(1) Coupling behavior along the X-direction:

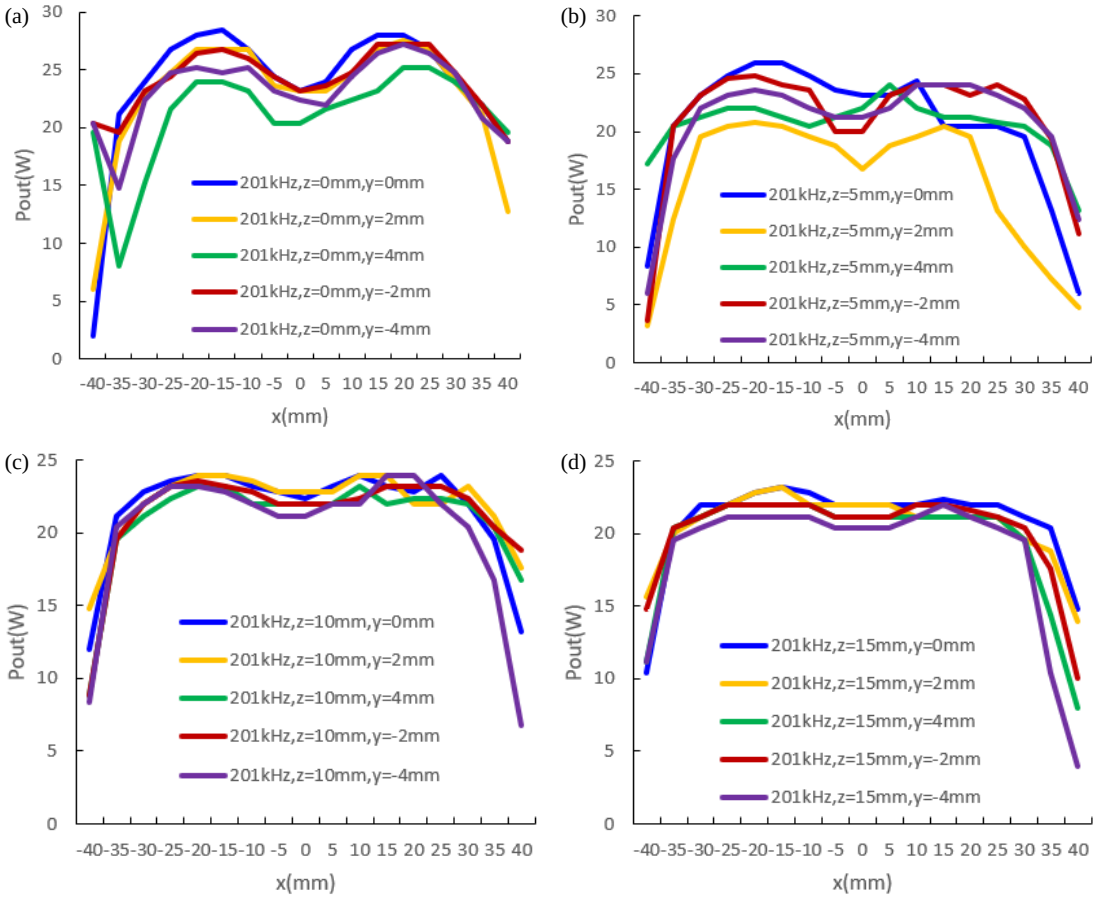

FIGURE 18. System output power characteristic curves under X-direction offset for (a) $Z = 0$ mm, (b) $Z = 5$ mm, (c) $Z = 10$ mm, and (d) $Z = 15$ mm, at $f = 201$ kHz.

TABLE 4. Transmission characteristics along the X-direction.

Operating frequency (kHz)	Z (mm)	Range (mm)	Maximum power (W)	Coordinates of the maximum power (mm)	Coordinates of the minimum power (mm)
191	15	−30–30	24.4	$Y = -2, X = -20$	$Z = 15, Y = -2$
	10		24.0	$Y = 2, X = 15$	$Z = 10, Y = 2$
	5		25.2	$Y = 0, X = -20$	$Z = 5, Y = 4$
	0		25.2	$Y = 0, X = -20$	$Z = 0, Y = -4$
196	15	−30–30	22.4	$Y = 0, X = 10$	$Z = 15, Y = -4$
	10	−25–25	24.0	$Y = 0, X = 10$	$Z = 10, Y = 4$
	5	−25–25	26.8	$Y = 5, X = -20$	$Z = 5, Y = 0$
	0	−20–20	28.4	$Y = 0, X = -15$	$Z = 0, Y = 0$
201	15	−30–30	23.2	$Y = 0, X = -15$	$Z = 15, Y = -4$
	10		23.6	$Y = 0, X = -25$	$Z = 10, Y = -4$
	5		24.8	$Y = 0$, X= -25	$Z = 5, Y = 2$
	0		28.4	$Y = 0, X = -15$	$Z = 0, Y = 0$

At $f = 191$ kHz, the stable operating range is extended to $X = \pm 30$ mm.

When the frequency reaches the critical coupling point ($f = 196$ kHz), this range is narrowed to $X = \pm 20$ mm. This presents a contraction attributed to the alignment of the coil self-resonant frequency.

At $f = 201$ kHz, the operating range is re-extended to $X = \pm 30$ mm, which indicates that the system enters an over-coupled state. In general, the X-direction offset demonstrates a "contraction-recovery" trend with frequency variation.

(2) Spatial stability along the Y-direction:

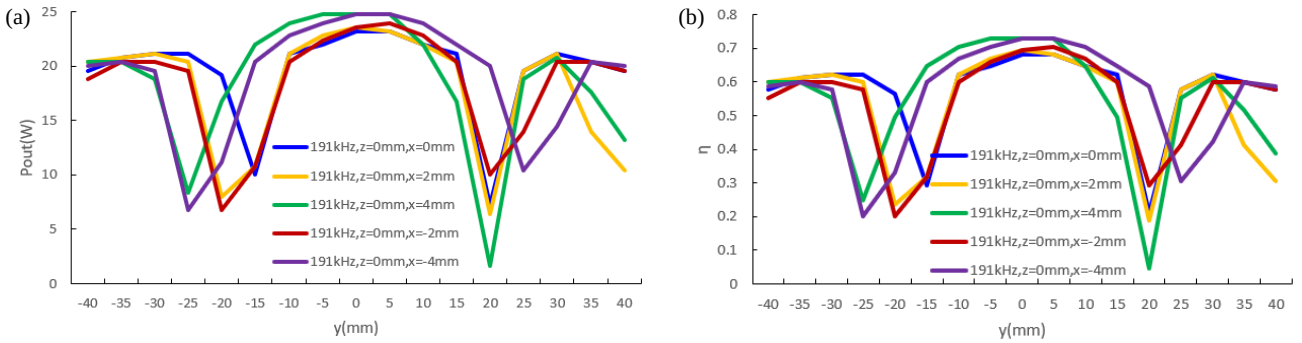

FIGURE 19. (a) Output power and (b) η under Y-direction offset at 191 kHz and $Z = 0$ mm.

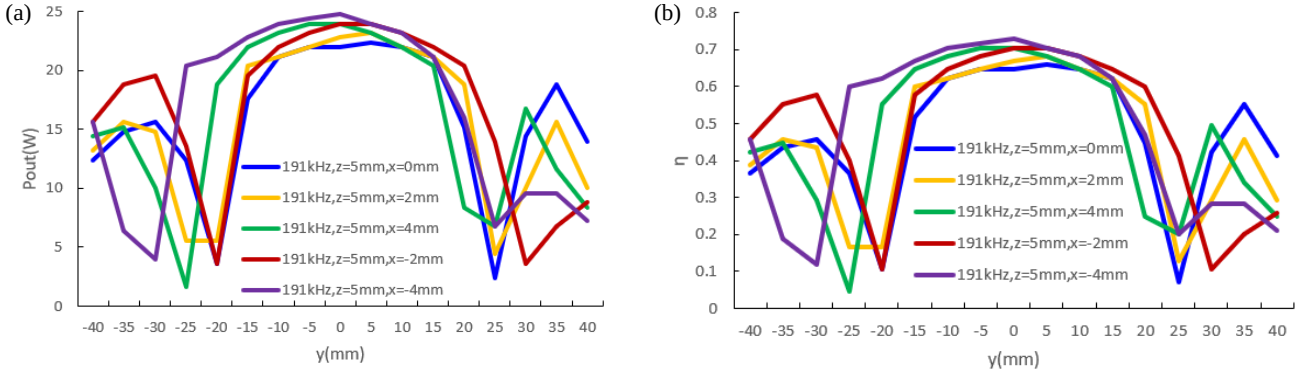

FIGURE 20. (a) Output power and (b) η under Y-direction offset at 191 kHz and $Z = 5$ mm.

TABLE 5. Transmission characteristics along the Y-direction.

Operating frequency (kHz)	Z (mm)	Stable range (mm)	Maximum power (W)	Coordinates of the maximum power (mm)	Coordinates of the minimum power (mm)
191	15	−20–20	24.4	$Y = -0, X = -4$	$Z = 15, X = -4$
	10		24.0	$Y = 0, X = -4$	$Z = 10, X = -2$
	5		25.2	$Y = 5, X = -4$	$Z = 5, X = 4$
	0		25.2	$Y = 0, X = -4$	$Z = 0, X = 4$
196	15	−20–20	22.4	$Y = 0, X = -4$	$Z = 15, X = 0$
	10		24.0	$Y = 0, X = -4$	$Z = 10, X = 4$
	5		26.8	$Y = 5, X = -4$	$Z = 5, X = -4$
	0		28.4	$Y = 0, X = -4$	$Z = 0, X = -2$
201	15	−20–20	23.2	$Y = 0, X = -4$	$Z = 15, X = 4$
	10		23.6	$Y = 0, X = -4$	$Z = 10, X = -2$
	5		24.8	$Y = 5, X = -4$	$Z = 5, X = -4$
	0		28.4	$Y = 0, X = -4$	$Z = 0, X = -2$

Regardless of the frequency, the stable range in the Y-direction remains constant at $Y = \pm 20$ mm. The 3D model confirms that the impact of the Y-direction offset on system coupling is spatially isotropic, verifying the magnetic-field uniformity provided by the two semicircular coil structures along the Y-axis. This result is consistent with the theoretical magnetic-circuit design.

(3) Spatial stability along the Z-direction:

Similarly, for all the tested frequencies, the stable range in the Z-direction is fixed at $Z = 0$–15 mm. Beyond this range, output power and η vary significantly.

4.4. Comparison with Related Coil Topologies

The performance of the proposed DSC coils is compared with those of DD, double DD, and double DDQ coils [16–20]. The obtained results are shown in Table 6. The DSC coils demon-

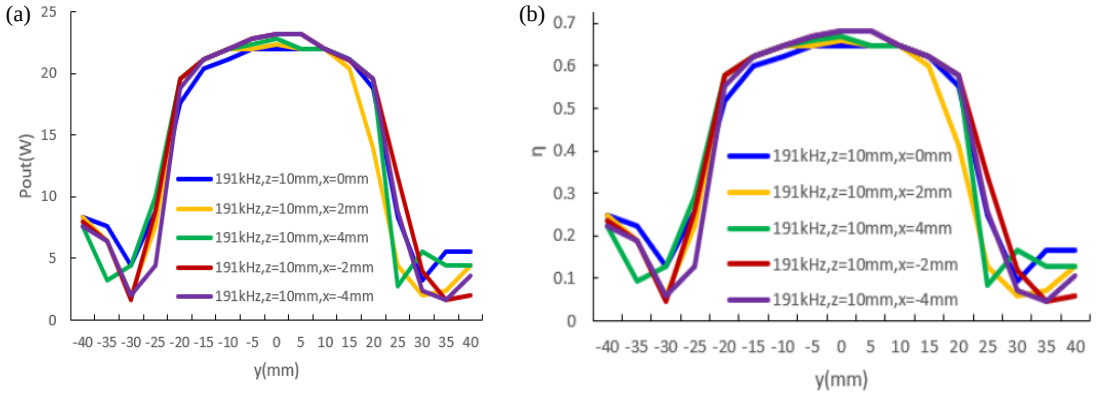

FIGURE 21. (a) Output power and (b) η under Y-direction offset at 191 kHz and $Z = 10$ mm.

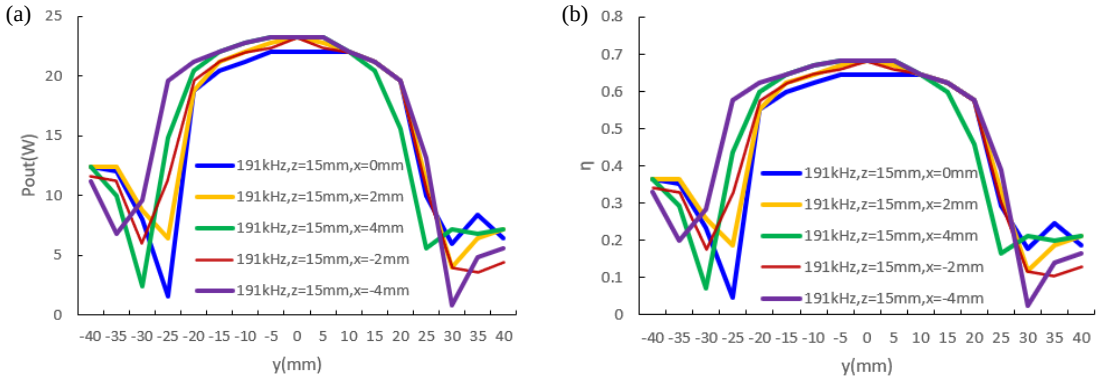

FIGURE 22. (a) Output power and (b) η under Y-direction offset at 19 kHz and $Z = 15$ mm.

TABLE 6. Comparison between the proposed DSC coils and existing DD-type ones.

Topology	DD	Double DD	DDQ	DSC
Coil size (mm)	100 × 100	100 × 100	100 × 100	Φ40
Operating frequency (kHz)	85	87	87	196
Transfer distance (mm)	15.3	15.3	10.0	0–15
Output power (W)	12.6	30.0	24.0	21.0–28.4
η (%)	83.7	83.3	60	80–85
Misalignment tolerance (mm)	X: ±25 Y: sensitive	X: ±25 Y: ±25	X: ±30 Y: ±30	X: ±30, Y: ±20, Z: 0–15

strate clear advantages in normalized misalignment tolerance and frequency stability. They achieve stable output power and η within a well-defined 3D spatial region, outperforming existing DD-type structures. This is attributed to their simple coplanar geometry, combining 3D spatial stability with frequency robustness.

5. DISCUSSION

In the proposed WPT system, a uniform magnetic field is achieved at the transmitting and receiving ends by employing DSC coils and a single Rx coil. This design ensures stable output power and η within a specific 3D spatial range. However, this improvement in misalignment tolerance comes at the expense of a reduced peak transmission efficiency compared with conventional WPT systems. It can be seen from the circuit diagram in Fig. 2 and the formula of η in Equation (7) that splitting the transmitting coil into two semicircular coils introduces mutual inductance between them. This has been observed many times in the denominator of the efficiency expression, which results in reducing the peak transmission efficiency.

Therefore, in future work, the structure of the DSC coils should be optimized, and new coil topologies should be derived based on its magnetic field constraint principle. This could increase η within its stable operating region. Fig. 25 shows coplanar symmetric topological coils. Several improved coil structures having higher transmission performance can be observed. These advancements are crucial for enabling reliable applications in offset-sensitive scenarios, such as mobile phone wireless charging.

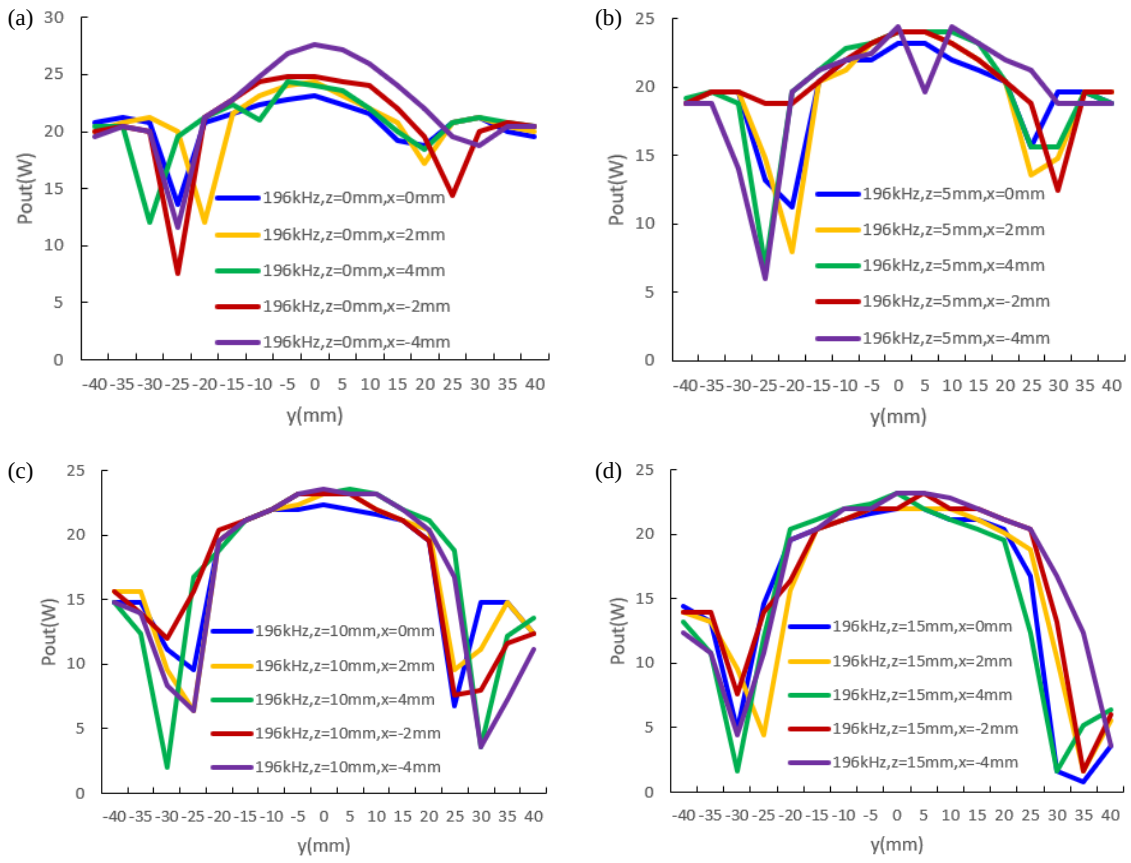

FIGURE 23. Output power under Y-offset at 196 kHz for transmission distances of (a) 0 mm, (b) 5 mm, (c) 10 mm, and (d) 15 mm.

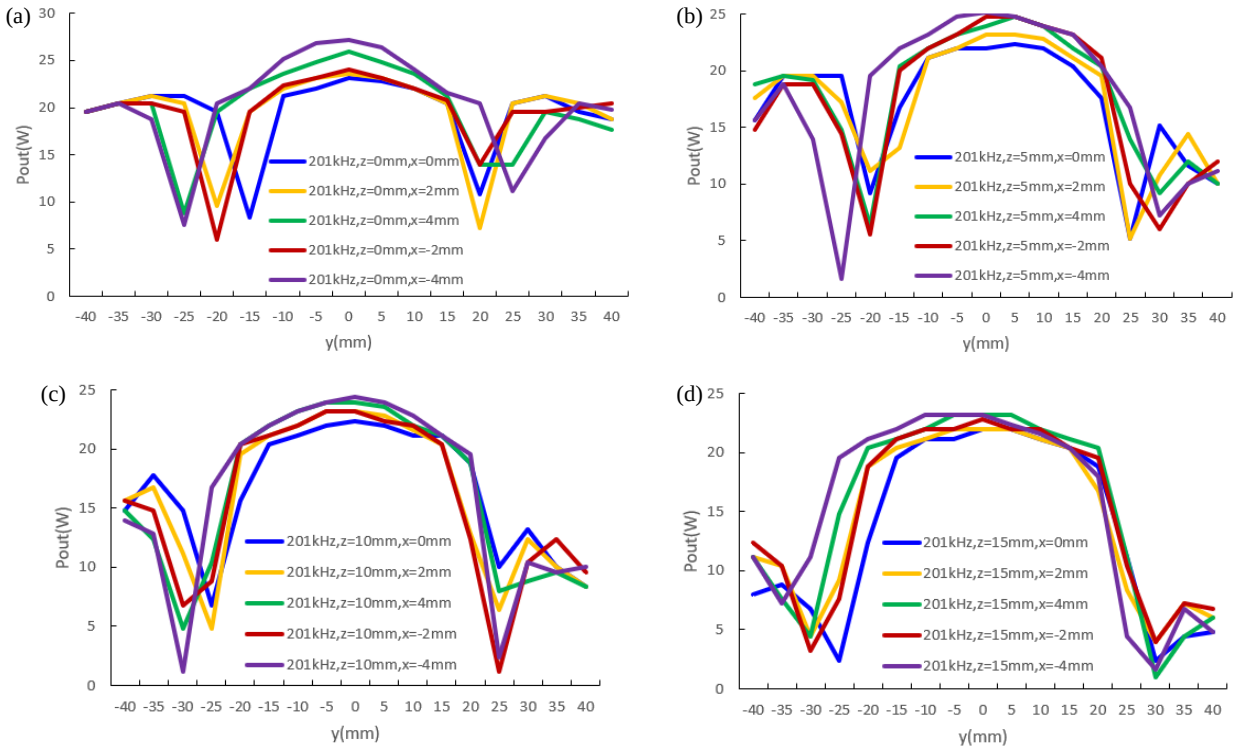

FIGURE 24. Output power under Y-offset at 201 kHz for transmission distances of (a) 0 mm, (b) 5 mm, (c) 10 mm, and (d) 15 mm.

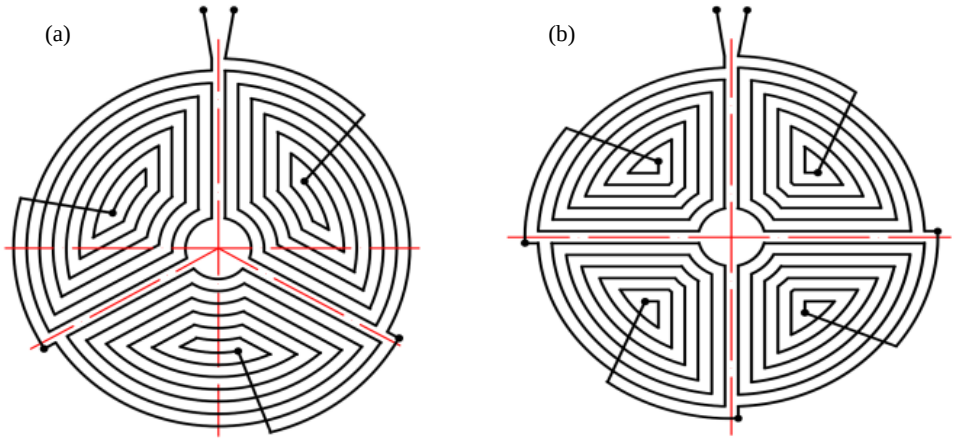

FIGURE 25. Coplanar symmetric topological coils: (a) one-third circular coplanar coil and (b) quarter-circular coplanar coil.

6. CONCLUSION

This study proposes a WPT topology employing DSC coils and a single receiver coil. It analyzes its performance characteristics through theoretical modeling, finite element simulation, and experimental verification.

The system generates a uniform magnetic field within a spatial range of $X = \pm 20$ mm, $Y = \pm 20$ mm, and $Z = 0$–15 mm through DSC coils, establishing a foundation for stable energy coupling and high misalignment tolerance. However, compared with conventional WPT structures, this design results in reducing the peak transmission efficiency.

Within the frequency band of 191–201 kHz, the system has high frequency stability. The magnetic field distribution has no significant variation, and the transmission efficiency follows a peak-stable trend. At 191 kHz and 201 kHz, the stable output power range in the X-direction remains at ± 30 mm. Even at the critical frequency of 196 kHz, where a critical coupling point occurs, this range is only narrowed to ± 20 mm.

The misalignment tolerance demonstrates 3D spatial characteristics: the stable range in the X-direction has a "contraction–recovery" behavior exhibiting frequency variation, while those in the Y-direction (± 20 mm) and Z-direction (0–15 mm) are stable. Within this cuboid region, which does not exceed half the outer diameter of the receiving coil, the output power and transmission efficiency slightly fluctuate in the ranges of 21–28.4 W and 4-27%, respectively. When the receiver offset exceeds half its diameter, the magnetic field uniformity and mutual inductance change abruptly, leading to a sudden variation in the output power and transmission efficiency.

The proposed topology provides a practical solution for offset-sensitive applications, such as mobile phone charging, allowing for effectively balancing the implementation complexity and system performance. It also provides a theoretical foundation and a parametric reference for the further optimization of WPT systems.

ACKNOWLEDGEMENT

This work was supported by the "Empowerment" Action Plan (Guangxi Key Research and Development Program) (2025FN96441019).

REFERENCES

[1] Tesla, N., "Apparatus for transmitting electrical energy," U.S. Patent, 1,119,732, 1914.

[2] Kurs, A., A. Karalis, R. Moffatt, J. D. Joannopoulos, P. Fisher, and M. Soljacic, "Wireless power transfer via strongly coupled magnetic resonances," *Science*, Vol. 317, No. 5834, 83–86, 2007.

[3] Chen, W., J. Liu, S. Chen, and L. Zhang, "Energy shaping control for wireless power transfer system in automatic guided vehicles," *Energies*, Vol. 13, No. 11, 2959, 2020.

[4] Khan, S. R., S. K. Pavuluri, G. Cummins, and M. P. Y. Desmulliez, "Miniaturized 3-D cross-type receiver for wirelessly powered capsule endoscopy," *IEEE Transactions on Microwave Theory and Techniques*, Vol. 67, No. 5, 1985–1993, 2019.

[5] Luo, Z. and X. Wei, "Analysis of square and circular planar spiral coils in wireless power transfer system for electric vehicles," *IEEE Transactions on Industrial Electronics*, Vol. 65, No. 1, 331–341, 2018.

[6] Kalwar, K. A., S. Mekhilef, M. Seyedmahmoudian, and B. Horan, "Coil design for high misalignment tolerant inductive power transfer system for EV charging," *Energies*, Vol. 9, No. 11, 937, 2016.

[7] Prosen, N., J. Domajnko, and M. Milanovič, "Wireless power transfer using double DD coils," *Electronics*, Vol. 10, No. 20, 2528, 2021.

[8] Domajnko, J. and N. Prosen, "A wireless power transfer system using a double DD quadrature coil structure," *Electronics*, Vol. 12, No. 4, 890, 2023.

[9] Domajnko, J. and N. Prosen, "A control of a z-axis rotation-tolerant wireless power transfer system using a double DD coil," *Electronics*, Vol. 12, No. 3, 606, 2023.

[10] Xie, J., G. Li, S. Jo, and D.-H. Kim, "A study on a fully integrated coil based on the LCCL-S compensation topology for wireless EVs charging systems," *Applied Sciences*, Vol. 13, No. 17, 9672, 2023.

[11] Abdulhameed, M., E. ElGhanam, A. H. Osman, and M. S. Hassan, "Design of a misalignment-tolerant inductor-capacitor-capacitor-compensated wireless charger for roadway-powered electric vehicles," *Sustainability*, Vol. 16, No. 2, 567, 2024.

[12] Liu, S. and Y. Liu, "Transfer characteristics of the MCR-WPT system using two series transmitting coils," *Circuit World*, Vol. 46, No. 1, 48–54, 2020.

[13] Liu, S., X. Yan, and Y. Liu, "Study on the two-load transmission characteristics of a WPT system with double transmitting coils," *Progress In Electromagnetics Research Letters*, Vol. 122, 67–74,

2024.

[14] Liu, S., J. Tan, and X. Wen, "Modeling of coupling mechanism of wireless power transfer system and vibration phenomenon of receiver-coil in three-coil system," *AIP Advances*, Vol. 7, No. 11, 115107, 2017.

[15] Liu, S. and J. Tan, "Study on the vibration mechanism of the relay coil in a three-coil WPT system," *Progress In Electromagnetics Research M*, Vol. 70, 117–126, 2018.

[16] Shen, T., Y. Yuan, L. Ling, H. Xu, J. Dong, and H. Ding, "The separated channel simultaneous wireless power and data transmission system based on double-layer orthogonal DD coils," in *2024 IEEE 4th International Conference on Data Science and Computer Application (ICDSCA)*, 1–6, Dalian, China, 2024.

[17] Chi, F., P. Wang, C. Sun, Y. Wu, Z. Dou, C. Xu, S. Wang, and W. Wang, "Research on optimization of horizontal omnidirectional misalignment tolerance of WPT based on double D coupler," *Electronics*, Vol. 11, No. 14, 2163, 2022.

[18] Chakibanda, V. and V. L. N. Komanapalli, "Core structure optimization in double-D coil with enhanced performance for inductive wireless power transfer system," *IEEE Access*, Vol. 12, 135 489–135 505, 2024.

[19] Zhuang, T., Y. Yao, Y. Yuan, Y. Wang, X. Liu, and D. Xu, "A DDQ/DD-coupler-based wireless power transfer system for electric vehicles charging featuring high misalignment tolerance," *Proceedings of the CSEE*, Vol. 42, No. 15, 5675–5684, 2022.

[20] Liu, Y. and J. Zhang, "Misalignment tolerance improvement and high efficiency design for wireless power transfer system based on DDQ-DD coil," *International Journal of Circuit Theory and Applications*, Vol. 52, No. 1, 111–128, 2024.